Switching Dynamic State Estimation and Event Detection for Inverter-Based Resources with Multiple Control Modes

Heqing Huang, *Student Member, IEEE*, Yuzhang Lin, *Member, IEEE*

***Abstract*—The Dynamic State Estimation (DSE) for Inverter-Based Resources (IBRs) is an emerging topic as IBRs gradually replace synchronous generators (SGs) in power systems. Unlike SGs, the dynamic models of IBRs heavily depend on their control algorithms, and conventional DSE methods for SGs, which assume a unchanged state space and dynamic model, cannot handle IBRs with control mode changes in real time, particularly when the power grid operators are unaware of the current control mode of the IBRs. In response to these challenges, an Expectation-Maximization Sliding-Window Iterated Extended Kalman Filter (EM-SW-IEKF) method is proposed in this paper. It theoretically achieves maximum likelihood estimation under different modes through the EM algorithm, providing the most probable control mode of the system as well as the corresponding state estimate. This method is validated in various IBR systems (battery energy storage systems and solar photovoltaic systems) and under different control mode transitions (switching between grid-following and grid-forming controls and between low voltage ride through and maximum power point tracking controls).**

***Index Terms*—switching model, dynamic state estimation, inverter-based resources, renewable energy, expectation-maximization algorithm, Kalman filter, grid-forming control, low voltage ride through mode**

I. Introduction

ALTHOUGH the replacement of traditional fossil-fuel generation with renewable energy generation, primarily Inverter-Based Resources (IBRs), has significantly benefited carbon emission reduction, new chanllenges have been introduced to the power systems as well [1]. The dynamics of IBRs significantly differ from traditional synchronous generators (SGs), characterized by being fast, inertia-less, heterogeneous, and distributed [2], [3]. These challenges must be taken care of by advanced monitoring and control technologies to maintain power system stability.

As a real-time monitoring technology enabled by granular sensor measurements, Dynamic State Estimation (DSE) has been widely studied for tracking the dynamics of SGs in power systems. Ref. [4] provides an overview of common DSE methods, among which are Extended Kalman Filter (EKF), Cubature Kalman Filter (CKF), Unscented Kalman Filter (UKF), Ensemble Kalman Filter (EnKF), and Particle Filter (PF), to name a few. In recent years, as IBRs increasingly become the focus of concern, the research on DSE for IBRs has been on a rising trend. Refs. [5] and [6] develop DSE for Doubly Fed Induction Generator based Wind Turbines (DFIG-WTs) and Permanent Magnet Synchronous Generator-based Wind Turbines (PMSG-WTs) using UKF and EKF, respectively. An adaptive CKF approach used in [7] achieves improved performance in DSE for PV systems. A DSE framework based on the EKF method, combined with consensus control, is proposed in Ref [8] for microgrids containing multiple Battery Energy Storage Systems (BESS). Not all inputs can be accurately measured in the DSE of IBRs. Ref. [9] employes the EKF with Unknown Input (EKF-UI) method to achieve the DSE of DFIGs when mechanical torque is unknown, while Ref. [10] uses the UKF-UI method for DSE under conditions of unknown wind speed. The methods mentioned above all follow the standard DSE architecture originally designed for SGs. Recognizing the essential difference between SGs and IBRs, Ref. [11] introduces a new framework for DSE for IBRs, which decouples the control subsystem from the physical subsystem to account for the signal uncertainty in between. Even though the DSE for IBRs is still an emerging area of research, it has already manifested the potential to enable new applications in the modeling, monitoring, control, protection of power systems [12]. For example, a fault detection method based on DSE for switching power inverters is presented in [13]; a frequency estimation and control method using IBRs, based on UKF, is proposed in [14]; a supplementary predictive control enabled by DSE to minimize transients in systems rich with IBRs is presented in [15].

Given that most dynamic behaviors of IBRs are determined by the digital controllers, all the DSE methods reviewed above model the control subsystem of the IBR and estimate its dynamics, in addition to the dynamics of the physical subsystem itself. An underlying assumption of all these existing methods is that the control mode of the IBR does not change, such that the IBR has an unchanged state space and dynamic model. However, this assumption is often unrealistic. For instance, as the voltage at the Point of Common Coupling (PCC) drops, IBRs often switch from the normal control mode to the Low Voltage Ride Through (LVRT) control mode, where certain state variables are restricted to prevent overcurrent conditions, and the model of the control subsystem changes [16], [17]. Another example of control mode change is that during main grid outages leading to unintentional islanding, some IBRs may switch from Grid Following (GFL) mode to Grid Forming (GFM) mode to support the continuous operation of the local grid [18]. In addition, as IBRs in the GFM mode can provide ancillary services to the grid [19], research has been undertaken for the optimal control mode selection for BESS based on the varying rates of electricity and auxiliary services [20]. It is obvious that *when IBRs switch between different*

control modes, their state spaces and dynamic models will change, and the existing DSE methods assuming an uniform state space and dynamic model are unable to recognize such changes and track system states effectively. In fact, as system operators who implement DSE do not have access to the internal information of IBR controllers, they are likely to be unaware of such control mode switching events. Therefore, *in addition to DSE itself, the detection of IBR control mode switching is another practical problem to address*.

Outside the power system domain, DSE methods that can handle switched system models have already found applications in various fields. Switching Kalman Filter (SKF) [21] is a typical method in this category. Ref. [22] uses SKF to identify and estimate the different dynamic modes in a communication network transmission environment, taking into account Denial-of-Service (DoS) attacks. SKF is also used for the processing of electrocardiogram signals with automatic selection of the most probable model [23]. Ref. [24] employs SKF to detect the most likely model for the aircraft health system and verifies its effectiveness. Similarly, Ref. [25] uses a robust SKF for lifespan analysis and verifies its reliability under non-Gaussian noise. This technique is also applied to corrosion detection for offshore wind turbines [26]. The combination of SKF with neural network technologies has led to the development of Switching Recurrent Kalman Networks [27] and a deep neural network switching Kalman filter [28] for pattern recognition technologies used in environments such as autonomous driving. A comprehensive review of various SKF techniques has been provided in Ref. [29].

Even though the SKF has been applied across various fields, it cannot be directly applied to the DSE for IBRs with control mode switching. *The primary issue lies in the assumption of SKF that different modes of a model share the same state space (i.e., the same set of state variables)*, typically differing only in the parameters of the state transition model or measurement model. However, this is not the case in the control mode switching of IBRs. For example, in the switching between GFL and GFM, the state variables under the two modes are completely different; upon operating in the LVRT mode, some state variables of IBRs are locked, leading to a change in the number of state variables. Therefore, for IBRs with mode switching, the state space may be completely changing, and only the output space is identical. These challenging situations cannot be handled by the existing SKF methods.

To address the aforementioned challenges, we propose a switching dynamic state estimation method, namly, the Expectation-Maximization Sliding-Window Iterated Extended Kalman Filter (EM-SW-IEKF),to accomplish *joint dynamic state estimation and control mode switching detection* for IBRs. The method employs the EM algorithm to solve the maximum likelihood estimation problem under varying control modes. By formulating a sliding-Window IEKF approach embedded into the EM framework, the stability and reliability of the method are enhanced, allowing for state estimation to be performed concurrently with control mode switching detection (control mode recognition). The main contributions are summarized as follows.

1) An EM-SW-IEKF method is proposed, enabling the detection of IBR mode switching events. The mode switching issue is transformed into a maximum likelihood estimation problem, solved by the EM algorithm to obtain the probabilities of each mode, thereby allowing the recognition of the control mode under a probabilistic framework. The reliability and stability of the method are enhanced by employing a sliding-window implementation.

2) The proposed EM-SW-IEKF method can accomplish continuous dynamic state estimation during control mode changes of IBRs, which cannot be accomplished by traditional DSE methods assuming an unchanged state space and dyanmic model of IBRs.

3) The EM-SW-EKF method is validated for various mode-switching scenarios of IBRs, including the switch between the GFL mode and the GFM mode, as well as the transition between the normal GFL mode and the LVRT mode.

The rest of the paper is organized as follows. Section II introduces the general IBR model with control mode switching, then presents the novel EM-SW-EKF method. Section III presents simulation results for various IBRs under different mode switching scenarios. Section IV concludes the paper.

II. Expectation-Maximization Sliding-Window Iterated Extended Kalman Filter

In order to derive the proposed method, it is first necessary for a general mathematical representation to be constructed, that is, the multi-mode state transition and measurement equations.

A. General Form of Dynamic Equations for IBR with Multiple Control Modes

Here, taking an IBR that switches between two different control modes as an example, the general state transition equation is as follows:

$$\begin{aligned} &\tfrac{d\mathbf{x}^{(i)}}{dt} = \mathbf{f}^{(i)}\left(\mathbf{x}^{(i)}, \mathbf{u}\right) + \mathbf{w}^{(i)}, i = 1, 2, ..., \kappa \\ &\mathbf{z} = \sum_{i=1}^{\kappa} c^{(i)} \cdot \mathbf{h}^{(i)}\left(\mathbf{x}^{(i)}, \mathbf{u}\right) + \mathbf{v}, \end{aligned} \tag{1}$$

where κ represents the total number of modes; $\mathbf{x}^{(i)} \in \mathbb{R}^{n_i \times 1}$ represents the state variables of mode i; $\mathbf{w}^{(i)} \in \mathbb{R}^{n_i \times 1}$ represents the process noise of mode i; $\mathbf{f}^{(i)}$ represents the state transition equation of mode i; $\mathbf{h}^{(i)}$ represents the output equation of mode i; $\mathbf{u} \in \mathbb{R}^{n_u \times 1}$ represents the external input, which includes all input signals of the κ control modes; $\mathbf{z} \in \mathbb{R}^{m_z \times 1}$ represents the measurement (system output), which is the same set of variables under different modes; $\mathbf{v} \in \mathbb{R}^{m_z \times 1}$ represents the measurement noise; $c^{(i)}$ is a random variable that takes the value of 0 or 1, with the probability of being 1 equal to $q^{(i)}$. Since the IBR can only be in one mode at any given time, it follows that $q^{(1)} + q^{(2)} + ... + q^{(\kappa)} = 1$ which follows a categorical distribution. There is often a lack of prior knowledge regarding the probability distribution of the modes: 1) the control modes may be determined by unmodeled external factors, such as the external grid condition or the IBR owner's behavior, which are not dependent on the IBR state; and 2) before knowing the mode, there is not a single set of state variables that can be used to derive the mode probability,

as the definition of the state space is dependent on the mode itself. Therefore, to reflect the lack of prior knowledge, a naive assignment of the prior estimate of $q^{(i)}$ can be adopted, e.g., each mode being assigned with the same prior probability. The posterior estimate of $q^{(i)}$ will be obtained by the proposed method after observations are made about the system (i.e., after measurements are received). Regarding the process noise and measurement noise, it is assumed that they both follow Gaussian distributions. Taking a simple case, such as $\kappa = 2$, then mode 1 and mode 2 could respectively represent the GFL mode and the GFM mode, or alternatively, the normal control mode and the LVRT mode, among other possibilities.

By contrast, the state transition equation for the problem solved by the traditional SKF method is as follows:

$$\begin{aligned} &\tfrac{d\mathbf{x}}{dt} = \sum_{i=1}^{\kappa} c^{(i)} \cdot \mathbf{f}^{(i)}\left(\mathbf{x}, \mathbf{u}\right) + \mathbf{w}, i = 1, 2, ..., \kappa \\ &\mathbf{z} = \mathbf{h}\left(\mathbf{x}, \mathbf{u}\right) + \mathbf{v}. \end{aligned} \tag{2}$$

Upon comparing Eq. (1) and Eq. (2), it is observed that in the control mode switching of an IBR, not only the state transition equations differ across modes, but also the definitions and quantities of state variables $\mathbf{x}^{(i)}$ may be entirely different. The SKF method primarily deals with DSE problems under conditions where the same state variables $\mathbf{x}$ exhibit different state transition equations (such as changes in parameters or fitting the actual nonlinear system using multiple linear models), as the model shown in (2). The state space, i.e., the number and definition of state variables in Eq. (2) are exactly the same under different modes, so the output equations in the problem solved by SKF do not change with different modes. All state variables exist and are observable by the outputs (i.e., measurements), if the outputs are configured properly. However, they are unable to handle the IBR systems with control mode changes, as the model shown in (1), where each mode is associated with a distinct state space, and when the system is in a certain mode, the state variables of the other modes become completely irrelevant to the outputs. They are either non-existent or unobservable in the actual system.

Discretizing (1) yields:

$$\begin{aligned} &\mathbf{x}_{(j)}^{(i)} = \mathbf{f}^{(i)}\left(\mathbf{x}_{(j-1)}^{(i)}, \mathbf{u}\right) + \mathbf{w}^{(i)}, i = 1, 2, ..., \kappa \\ &\mathbf{z}_{(j)} = \sum_{i=1}^{\kappa} c^{(i)} \cdot \mathbf{h}^{(i)}\left(\mathbf{x}_{(j)}^{(i)}, \mathbf{u}\right) + \mathbf{v}, \end{aligned} \tag{3}$$

where j represents jth time step. As previously mentioned, using only a single point of measurement for mode detection may lead to unreliable results due to the uncertainty of measurements. Therefore, measurements over a period of time can be selected to form a sliding window, and the measurements within this time window can be used for mode detection. Eq. (3)in a sliding window can be consolidated as:

$$\begin{cases} \mathbf{x}_{(1)}^{(i)} = \mathbf{f}^{(i)}\left(\mathbf{x}_{(0)}^{(i)+}, \mathbf{u}_{(0)}\right) + \mathbf{w}_{(1)}^{(i)}, \\ \mathbf{x}_{(2)}^{(i)} = \mathbf{f}^{(i)}\left(\mathbf{x}_{(1)}^{(i)}, \mathbf{u}_{(1)}\right) + \mathbf{w}_{(2)}^{(i)}, \\ ... \\ \mathbf{x}_{(N)}^{(i)} = \mathbf{f}^{(i)}\left(\mathbf{x}_{(N-1)}^{(i)}, \mathbf{u}_{(N-1)}\right) + \mathbf{w}_{(N-1)}^{(i)}. \end{cases} \tag{4}$$

where N the number of time steps (measurement points) within the time window; n inside the subscript brackets indicates the nth point within the time window, $\mathbf{u}_{(0)}$ is the input at the last time step of the previous sliding window; $\mathbf{x}_{(0)}^{(i)+}$ is the last point in the previous time window, with its covariance matrix being obtainable from the DSE of the previous time window, which is assumed to be $\mathbf{P}_{(0)}^{(i)+}$.

Eq. (4) can be transformed into the following form:

$$\mathbf{0}^{(i)} = \bar{\mathbf{x}}^{(i)} - \bar{\mathbf{f}}^{(i)}\left(\bar{\mathbf{x}}^{(i)}, \bar{\mathbf{u}}, \mathbf{x}_{(0)}^{(i)+}\right) + \bar{\mathbf{w}}^{(i)}, i = 1, 2, ..., \kappa \tag{5}$$

where $\bar{\mathbf{x}}^{(i)} = \left[\mathbf{x}_{(1)}^{(i)}; \mathbf{x}_{(2)}^{(i)}; ...; \mathbf{x}_{(N)}^{(i)}\right]$ is concatenated state vector within the sliding window, with the dimension being $n_i N \times 1$; similarly, $\bar{\mathbf{u}} = \left[\mathbf{u}_{(0)}; \mathbf{u}_{(1)}; ...; \mathbf{u}_{(N-1)}\right]$ and $\bar{\mathbf{w}}^{(i)} = \left[\mathbf{w}_{(1)}^{(i)}; \mathbf{w}_{(2)}^{(i)}; ...; \mathbf{w}_{(N)}^{(i)}\right]$ represent the concatenated input and process noise vectors, respectively; $\bar{\mathbf{f}}^{(i)}$ represents the concatenated state transition equation of mode i within sliding window; $\mathbf{0}^{(i)}$ is a zero vector having the same dimension as $\bar{\mathbf{x}}^{(i)}$; $\mathbf{x}_{(0)}^{(i)+}$ is the last point in the previous time window, with its covariance matrix to be $\mathbf{P}_{(0)}^{(i)+}$ represents the augmented state transition equation of mode i.

Eq. (5) provides constraints on the state variables by the state transition equations within the sliding window, while the constraints by the measurements are determined by the measurement (output) equation, which is as follows:

$$\bar{\mathbf{z}} = \sum_{i=1}^{\kappa} c^{(i)} \cdot \bar{\mathbf{h}}^{(i)}\left(\bar{\mathbf{x}}^{(i)}, \bar{\mathbf{u}}\right) + \bar{\mathbf{v}}, \tag{6}$$

where $\bar{\mathbf{z}} = \left[\mathbf{z}_{(1)}; \mathbf{z}_{(2)}; ...; \mathbf{z}_{(N)}\right]$ is the concatenated measurement vector of the sliding window, with the dimension being $m_z N \times 1$ and $\bar{\mathbf{v}} = \left[\mathbf{v}_{(1)}; \mathbf{v}_{(2)}; ...; \mathbf{v}_{(N)}\right]$ is the concatenated measurement (output) noise; $\bar{\mathbf{h}}^{(i)}$ represent the concatenated measurement (output) equations for control mode i.

It can be observed that the zero on the left side of each equation in (5) can also be considered as a form of measurement (pseudo-measurement). Therefore, by multiplying both sides of the ith equation in (5) by $c^{(i)}$ and combining it with (6), a unified augmented expression can be formed:

$$\tilde{\mathbf{z}} = \sum_{i=1}^{\kappa} c^{(i)} \cdot \tilde{\mathbf{h}}_i\left(\tilde{\mathbf{x}}_i, \tilde{\mathbf{u}}\right) + \tilde{\mathbf{v}}, \tag{7}$$

where $\tilde{\mathbf{z}} = \left[\bar{\mathbf{z}}; \mathbf{0}^{(1)}; \mathbf{0}^{(2)}; ...; \mathbf{0}^{(\kappa)}\right]$ represents the augmented measurement vector with actual measurements and pseudo-measurements given by state transition; $\tilde{\mathbf{v}} = \left[\bar{\mathbf{v}}; c^{(1)}\bar{\mathbf{w}}^{(1)}; c^{(2)}\bar{\mathbf{w}}^{(2)}; ...; c^{(\kappa)}\bar{\mathbf{w}}^{(\kappa)}\right]$ represents the augmented noise including output noise and process noise; $\tilde{\mathbf{u}}$ represents all the inputs including $\bar{\mathbf{u}}$ and $\mathbf{x}_{(0)}^{(1)+}$ to $\mathbf{x}_{(0)}^{(\kappa)+}$. $\tilde{\mathbf{x}}^{(i)}$ is the same as $\bar{\mathbf{x}}^{(i)}$. $\tilde{\mathbf{h}}^{(i)} = \left[\bar{\mathbf{h}}^{(i)}; \mathbf{0}^{(1)}; ...; \mathbf{0}^{(i-1)}; \tilde{\mathbf{f}}^{(i)}; \mathbf{0}^{(i+1)}; ...; \mathbf{0}^{(\kappa)}\right]$ is the augmented measurement equations that incorporate the state transition and output equations, where $\tilde{\mathbf{f}}^{(i)}\left(\tilde{\mathbf{x}}^{(i)}, \tilde{\mathbf{u}}\right) = \tilde{\mathbf{x}}^{(i)} - \bar{\mathbf{f}}^{(i)}\left(\tilde{\mathbf{x}}^{(i)}, \tilde{\mathbf{u}}\right)$. For $\tilde{\mathbf{h}}^{(i)}$, the parts corresponding to the state transition equations of modes other than mode i are all zero.

B. Maximum Likelihood Estimation and the EM Algorithm

Through the derivation process described above, an augmented measurement equation for the multi-control mode

IBR, combining the state transition equation and the actual measurement (output) equation, is obtained as shown in Eq. (7). Assuming that both the measurement (output) noise and the process noise are independent Gaussian white noise with a mean of zero, $\tilde{\mathbf{v}} \in N\left(0, \sigma^2\right)$, the covariance matrix of $\tilde{\mathbf{v}}$ is a block diagonal matrix, consisting of the covariance matrix of the measurement (output) noise $\mathbf{R}$ and the covariance matrix of the process noise for mode i (which is $c^{(i)} \cdot \mathbf{Q}^{(i)}$) as its diagonal blocks. Then the probability density function (PDF) of augmented measurements can be expressed as follows:

$$p\left(\tilde{\mathbf{z}}\right) = \sum_{i=1}^{\kappa} q^{(i)} \cdot p\left(\tilde{\mathbf{z}} | \, \tilde{\mathbf{h}}^{(i)}\left(\tilde{\mathbf{x}}^{(i)}, \tilde{\mathbf{u}}\right)\right), \tag{8}$$

where $p\left(\tilde{\mathbf{z}}\right)$ represents the PDF of $\tilde{\mathbf{z}}$.

Given $\tilde{\mathbf{z}}$, the likelihood function can be formulated into:

$$L\left(\tilde{\mathbf{x}}^{(1)}, \tilde{\mathbf{x}}^{(2)}, ..., \tilde{\mathbf{x}}^{(\kappa)}, q^{(1)}, q^2, ..., q^{(\kappa)}\right) = \log\left(p\left(\tilde{\mathbf{z}}\right)\right). \tag{9}$$

Therefore, the maximum likelihood estimation of $\tilde{\mathbf{x}}^{(1)}, \tilde{\mathbf{x}}^{(2)}, ..., \tilde{\mathbf{x}}^{(\kappa)}$ and $q^{(1)}, q^2, ..., q^{(\kappa)}$ is to find:

$$[\hat{\mathbf{x}}, \hat{q}] = \arg\max_{\tilde{\mathbf{x}}, q}\left(\log\left(\sum_{i=1}^{\kappa} q^{(i)} \cdot p\left(\tilde{\mathbf{z}} | \, \tilde{\mathbf{h}}^{(i)}\left(\tilde{\mathbf{x}}^{(i)}, \tilde{\mathbf{u}}\right)\right)\right)\right), \tag{10}$$

where $\hat{\mathbf{x}}$ represents all dynamic state variables $\left[\hat{\mathbf{x}}^{(1)}, \hat{\mathbf{x}}^{(2)}, ..., \hat{\mathbf{x}}^{(\kappa)}\right]$ and $\hat{q}$ represents all the mode probabilities $\left[\hat{q}^{(1)}, \hat{q}^{(2)}, ..., \hat{q}^{(\kappa)}\right]$. The mode with the highest probability can be deemed the detected control mode of the IBR. It is challenging to solve (10) directly.

The EM algorithm is a powerful statistical tool for finding maximum likelihood estimates of parameters in probabilistic models such as (10). The EM algorithm consists of two steps, namely the Expectation (E) step and the Maximization (M) step.

1) Expectation step: The Q function is defined as the expected value of the log-likelihood function with respect to the current conditional distribution of the given measurements $\tilde{\mathbf{z}}$ and the current estimates of the parameters $\hat{\mathbf{x}}$ and $\hat{q}$:

$$Q\left(\tilde{\mathbf{x}}, \tilde{q}\right) = E\left(\log\left(\sum_{i=1}^{\kappa} q^{(i)} \cdot p\left(\tilde{\mathbf{z}} | \, \tilde{\mathbf{h}}^{(i)}\left(\tilde{\mathbf{x}}^{(i)}, \tilde{\mathbf{u}}\right)\right)\right)\right). \tag{11}$$

By utilizing the definition of expectation, $E\left(x\right) = \sum_{i=1}^{\kappa} x_i p\left(x_i\right)$, it can be transformed into:

$$\begin{aligned} Q &= \sum_{i=1}^{\kappa} p\left(c^{(i)} = 1 \, | \tilde{\mathbf{z}}\right) \cdot \log\left[p\left(\tilde{\mathbf{z}} \left| c^{(i)} = 1\right.\right) p\left(c^{(i)} = 1\right)\right] \\ &= \sum_{i=1}^{\kappa} w^{(i)} \cdot \log\left[p\left(\tilde{\mathbf{z}} \left| c^{(i)} = 1\right.\right) p\left(c^{(i)} = 1\right)\right], \end{aligned} \tag{12}$$

where $w^{(i)}$ is called the *membership probabilities* of each mode, typically considered as the output of the Expectation step. By using the formula for conditional probability, the expression for membership probabilities can be obtained:

$$w^{(i)} = p\left(c^{(i)} = 1 \, | \tilde{\mathbf{z}}\right) = \frac{p\left(\tilde{\mathbf{z}} \left| c^{(i)} = 1\right.\right) p\left(c^{(i)} = 1\right)}{\sum_{l=1}^{\kappa} p\left(\tilde{\mathbf{z}} \left| c^{(l)} = 1\right.\right) p\left(c^{(l)} = 1\right)}, \tag{13}$$

where $p\left(c^{(i)} = 1\right) = \hat{q}^{(i)}$. To solve Eq. (13), it is also necessary to know all the probabilities $p\left(\tilde{\mathbf{z}} \left| c^{(l)} = 1\right.\right)$ for l from 1 to κ. Observing (7), it is noted that when $c^{(i)} = 1$, aside from the measurement item ($\bar{\mathbf{z}}$ in $\tilde{\mathbf{z}}$) and the pseudo-measurement item corresponding to the state transition equation of the ith mode ($\mathbf{0}^{(i)}$ in $\tilde{\mathbf{z}}$), the equations constructed from the state transition equations of the other modes have both sides equal to zero. Therefore, it does not affect the PDF of $p\left(\tilde{\mathbf{z}} \left| c^{(i)} = 1\right.\right)$. Furthermore, since the measurement noise and process noise within the time window are independent Gaussian white noises, the conditional probability density distribution follows a Gaussian distribution given by:

$$\begin{aligned} &p\left(\tilde{\mathbf{z}} \left| \, c^{(i)} = 1\right.\right) = p\left(\tilde{\mathbf{z}} | \, \tilde{\mathbf{h}}^{(i)}\left(\tilde{\mathbf{x}}^{(i)}, \tilde{\mathbf{u}}\right)\right) \\ &= \varpi^{(i)} e^{-\left\|\mathbf{R}^{-\frac{1}{2}}\left(\bar{\mathbf{z}} - \tilde{\mathbf{h}}^{(i)}\left(\tilde{\mathbf{x}}^{(i)}, \tilde{\mathbf{u}}\right)\right)\right\|_2^2 - \left\|\left(\mathbf{Q}^{(i)}\right)^{-\frac{1}{2}}\left(\mathbf{0} - \tilde{\mathbf{f}}^{(i)}\left(\tilde{\mathbf{x}}^{(i)}, \tilde{\mathbf{u}}\right)\right)\right\|_2^2}, \end{aligned} \tag{14}$$

where:

$$\varpi^{(i)} = \frac{1}{\left(\sqrt{2\pi}\right)^{m_z N + n_i N}\sqrt{|\mathbf{R}|}\sqrt{\left|\mathbf{Q}^{(i)}\right|}}. \tag{15}$$

2) Maximization step: The Maximization step assumes that the membership probabilities, which have been calculated in Expectation step, are known, and estimates the state variables and the parameters q. This is done by maximizing a convex lower bound J of the Q function:

$$J\left(\hat{\mathbf{x}}, \hat{q}\right) = \sum_{i=1}^{\kappa} w^{(i)} \cdot \log\left(p\left(\tilde{\mathbf{z}} \left| c^{(i)} = 1\right.\right) p\left(c^{(i)} = 1\right)\right). \tag{16}$$

Substituting (14) and (15) into (16) yields:

$$\begin{aligned} &\left(\hat{\mathbf{x}}, \hat{q}\right) = \arg\min\left(J\left(\tilde{\mathbf{x}}, \tilde{q}\right)\right) = \\ &\sum_{i=1}^{\kappa} w^{(i)}\left(\log\left(\frac{1}{\left(\sqrt{2\pi}\right)^{m_z N}\sqrt{|\mathbf{R}|}}\right) + \log\left(\frac{1}{\left(\sqrt{2\pi}\right)^{n_i N}\sqrt{\left|\mathbf{Q}^{(i)}\right|}}\right)\right) \\ &+ \sum_{i=1}^{\kappa} w^{(i)}\left(\log\left(q^{(i)}\right)\right) \\ &- \sum_{i=1}^{\kappa} w^{(i)}\left(\begin{array}{l} \left\|\mathbf{R}^{-\frac{1}{2}}\left(\bar{\mathbf{z}} - \bar{\mathbf{h}}^{(i)}\left(\tilde{\mathbf{x}}^{(i)}, \tilde{\mathbf{u}}\right)\right)\right\|_2^2 + \\ \left\|\left(\mathbf{Q}^{(i)}\right)^{-\frac{1}{2}}\left(\mathbf{0} - \tilde{\mathbf{f}}^{(i)}\left(\tilde{\mathbf{x}}^{(i)}, \tilde{\mathbf{u}}\right)\right)\right\|_2^2 \end{array}\right). \end{aligned} \tag{17}$$

Observing (17), it is noted that the first term is constant, and the last two terms are independent of each other. More importantly, *in the last term, the weighted-least-square terms of each mode $i = 1$ to κ are independent from each other, thus can be minimized independently.* Therefore, maximizing J can be divided into two steps:

a) Individual state estimation for each mode $i = 1$ to κ:

$$\min_{\tilde{\mathbf{x}}^{(i)}}\left\{\begin{array}{l} \left\|\mathbf{R}^{-\frac{1}{2}}\left(\bar{\mathbf{z}} - \bar{\mathbf{h}}^{(i)}\left(\tilde{\mathbf{x}}^{(i)}, \tilde{\mathbf{u}}\right)\right)\right\|_2^2 + \\ \left\|\left(\mathbf{Q}^{(i)}\right)^{-\frac{1}{2}}\left(\mathbf{0} - \tilde{\mathbf{f}}^{(i)}\left(\tilde{\mathbf{x}}^{(i)}, \tilde{\mathbf{u}}\right)\right)\right\|_2^2 \end{array}\right\}. \tag{18}$$

b) Probability estimation by differentiating the objective function with respect to q and equating it to zero based on the constraint $w^{(1)} + w^{(2)} + ... + w^{(\kappa)} = 1$:

$$\frac{\partial J}{\partial q} \Rightarrow q^{(i)} = w^{(i)}. \tag{19}$$

The EM algorithm is deemed convergent when the difference between the objective function values of two consecutive iterations is lower than a threshold. However, it is surprisingly found that, according to Eq. (17), the state estimation of each mode is not dependent on the probability of the mode, even though the probability of the mode is dependent on the state estimation result. Therefore, in this case, the entire EM algorithm can be completed by first assuming a set of prior values of $q^{(i)}$, then performing DSE for each mode, and finally obtaining the posterior values of $q^{(i)}$ based on the obtained state variables. There is no need to repeat the DSE for each mode after $q^{(i)}$ is updated. Therefore, no iterative computation is required.

It can be observed that in order to use the EM algorithm to obtain the probability of the IBR operating in mode k, it is first necessary to solve κ Weighted Least Squares (WLS) problems of the form presented in Eq. (18), finding the state estimate $\hat{\mathbf{x}}_k$ of each mode $i = 1$ to κ. Notably, according to Ref. [30], the well-known DSE method for dynamical systems with a single mode, IEKF, can be transformed into a WLS problem using the Matrix Inversion Lemma (MIL) and the Gain Expression (GE) Identity. For nonlinear systems, this equivalent WLS problem for a sliding window can be expressed as [31]:

$$\min_{\tilde{\mathbf{x}}^{(i)}} \left\{ \begin{array}{l} \left(\bar{\mathbf{z}} - \bar{\mathbf{h}}^{(i)}\left(\tilde{\mathbf{x}}^{(i)}, \tilde{\mathbf{u}}\right)\right)^T \mathbf{R}^{-1} \left(\bar{\mathbf{z}} - \bar{\mathbf{h}}^{(i)}\left(\tilde{\mathbf{x}}^{(i)}, \tilde{\mathbf{u}}\right)\right) + \\ \left(\mathbf{0} - \tilde{\mathbf{f}}^{(i)}\left(\tilde{\mathbf{x}}^{(i)}, \tilde{\mathbf{u}}\right)\right)^T \left(\mathbf{Q}^{(i)}\right)^{-1} \left(\mathbf{0} - \tilde{\mathbf{f}}^{(i)}\left(\tilde{\mathbf{x}}^{(i)}, \tilde{\mathbf{u}}\right)\right) \end{array} \right\} \tag{20}$$

It can be found that Eq. (20) and Eq. (18) are the same. Consequently, an elegant conclusion is reached: part of the Maximization step of the EM algorithm for IBRs with κ modes is equivalent to solving κ sliding-window IEKF (SW-IEKF) expressed in the WLS form (20). In other words, it can be assumed that the measurements originate from each mode $i = 1$ to κ and solve the standard SW-IEKF problem in the WLS form (20). Afterwards, utilizing the state estimates obtained from solving the WLS problems, the probabilities of each mode can be evaluated by (19), another part of the Maximization step of the EM algorithm, then mode detection/recognition can be completed by choosing the mode with the highest probability. Another beauty of this conclusion is that the SW-IEKF problem for each mode Eq. (20) is an independent computation task. Hence, parallel computing may be applied to each node should there be a computational need.

C. Sliding-Window Iterated Extended Kalman Filter

As discussed above, the proposed EM algorithm embeds a step where κ instances of SW-IEKF should be solved. Here, we introduce the process of SW-IEKF for any $i = 1$ to κ.

1) Initialization. Obtain all measurements within the sliding window $\bar{\mathbf{z}} = \left[\mathbf{z}_{(1)}; \mathbf{z}_{(2)}; ...; \mathbf{z}_{(N)}\right]$; obtain the state variable of the last time step from the previous sliding window, designated as $\mathbf{x}_{(0)}^{(i)+}$; use the state transition equation to recursively derive the initial estimates of all dynamic state variables within the sliding window $\hat{\mathbf{x}}^{(i)(0)}$ where the superscript 0 indicates the estimate after the 0th iteration.

2) Prediction. Using (4), we can obtain the prior estimates of thestate variables $\hat{\mathbf{x}}^{(i)(0-)} = \left[\hat{\mathbf{x}}_{(1)}^{(i)(0-)}; \hat{\mathbf{x}}_{(2)}^{(i)(0-)}; ...; \hat{\mathbf{x}}_{(N)}^{(i)(0-)}\right]$.

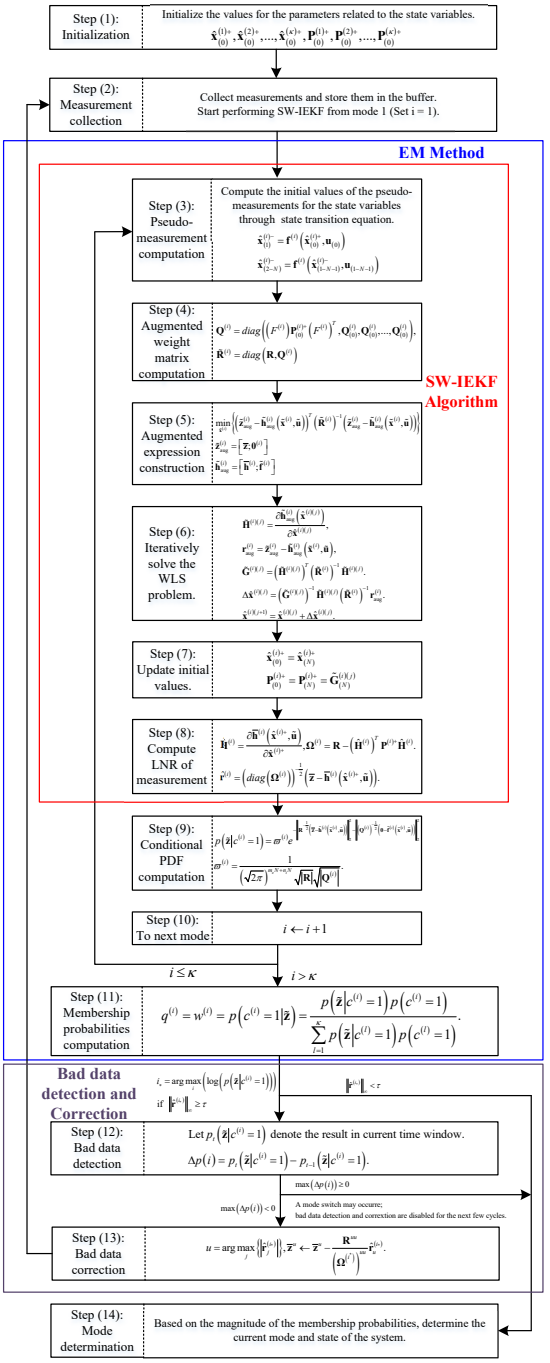

Fig. 1. Proposed EM-SW-IEKF algorithm.

After converting it to the form of (5), obtain the covariance matrix of the prior estimates within the sliding window:

$$\mathbf{Q}^{(i)} = diag\left(\left(\mathbf{F}^{(i)}\right)\mathbf{P}_{(0)}^{(i)+}\left(\mathbf{F}^{(i)}\right)^T, \mathbf{Q}_{(0)}^{(i)}, \mathbf{Q}_{(0)}^{(i)}, ..., \mathbf{Q}_{(0)}^{(i)}\right), \tag{21}$$

wherein the first item of the block diagonal matrix $\mathbf{Q}^{(i)}$ is a product of $\mathbf{F}^{(i)}$, the Jacobian matrix of $\mathbf{f}^{(i)}$, and $\mathbf{P}_{(0)}^{(i)+}$, the posterior covariance of $\mathbf{x}_{(0)}^{(i)+}$; the remaining $N-1$ items are $\mathbf{Q}_{(0)}^{(i)}$, the process noise covariance of mode i.

3) Correction. To facilitate the solution to (20), it can be

rewritten in the following form:

$$\hat{\mathbf{x}}^{(i)+} = \arg\min_{\tilde{\mathbf{x}}^{(i)}} \left\{ \begin{array}{l} \left(\left[\begin{array}{c} \bar{\mathbf{z}} \\ \mathbf{0} \end{array} \right] - \left[\begin{array}{c} \bar{\mathbf{h}}^{(i)}\left(\tilde{\mathbf{x}}^{(i)}, \tilde{\mathbf{u}}\right) \\ \tilde{\mathbf{f}}^{(i)}\left(\tilde{\mathbf{x}}^{(i)}, \tilde{\mathbf{u}}\right) \end{array} \right] \right)^T \\ \cdot \left[\begin{array}{cc} \mathbf{R} & \\ & \mathbf{Q}^{(i)} \end{array} \right]^{-1} \\ \cdot \left(\left[\begin{array}{c} \bar{\mathbf{z}} \\ \mathbf{0} \end{array} \right] - \left[\begin{array}{c} \bar{\mathbf{h}}^{(i)}\left(\tilde{\mathbf{x}}^{(i)}, \tilde{\mathbf{u}}\right) \\ \tilde{\mathbf{f}}^{(i)}\left(\tilde{\mathbf{x}}^{(i)}, \tilde{\mathbf{u}}\right) \end{array} \right] \right) \end{array} \right\}$$
$$= \arg\min_{\tilde{\mathbf{x}}^{(i)}} \left\{ \begin{array}{l} \left(\tilde{\mathbf{z}}_{\text{aug}}^{(i)} - \tilde{\mathbf{h}}_{\text{aug}}^{(i)}\left(\tilde{\mathbf{x}}^{(i)}, \tilde{\mathbf{u}}\right) \right)^T \left(\tilde{\mathbf{R}}^{(i)} \right)^{-1} \\ \cdot \left(\tilde{\mathbf{z}}_{\text{aug}}^{(i)} - \tilde{\mathbf{h}}_{\text{aug}}^{(i)}\left(\tilde{\mathbf{x}}^{(i)}, \tilde{\mathbf{u}}\right) \right) \end{array} \right\}, \tag{22}$$

where $\tilde{\mathbf{z}}_{\text{aug}}^{(i)} = \left[\bar{\mathbf{z}}; \mathbf{0}^{(i)}\right]$ is the part of $\tilde{\mathbf{z}}$ that extracts the pseudo-measurements related to mode i; $\tilde{\mathbf{h}}_{\text{aug}}^{(i)} = \left[\bar{\mathbf{h}}^{(i)}; \tilde{\mathbf{f}}^{(i)}\right]$ is the part of $\tilde{\mathbf{h}}^{(i)}$; $\tilde{\mathbf{R}}^{(i)} = diag\left(\mathbf{R}, \mathbf{Q}^{(i)}\right)$. The Gauss-Newton method can be used for solving this problem as follows.

3.1) Set iteration number $j = 0$ and setstate estimate tolerance τ. Initialize the state variables $\hat{\mathbf{x}}^{(i)(j)} = \hat{\mathbf{x}}^{(i)(0-)}$.

3.2) The Jacobian matrix, augmented residuals and the gain matrix are evaluated as follows:

$$\tilde{\mathbf{H}}^{(i)(j)} = \frac{\partial \tilde{\mathbf{h}}_{\text{aug}}^{(i)}\left(\hat{\mathbf{x}}^{(i)(j)}\right)}{\partial \hat{\mathbf{x}}^{(i)(j)}}, \tag{23}$$

$$\mathbf{r}_{\text{aug}}^{(i)} = \tilde{\mathbf{z}}_{\text{aug}}^{(i)} - \tilde{\mathbf{h}}_{\text{aug}}^{(i)}\left(\tilde{\mathbf{x}}^{(i)}, \tilde{\mathbf{u}}\right), \tag{24}$$

$$\tilde{\mathbf{G}}^{(i)(j)} = \left(\tilde{\mathbf{H}}^{(i)(j)}\right)^T \left(\tilde{\mathbf{R}}^{(i)}\right)^{-1} \tilde{\mathbf{H}}^{(i)(j)}. \tag{25}$$

3.3) Compute the update value of the state variables:

$$\Delta\hat{\mathbf{x}}^{(i)(j)} = \left(\tilde{\mathbf{G}}^{(i)(j)}\right)^{-1} \tilde{\mathbf{H}}^{(i)(j)} \left(\tilde{\mathbf{R}}^{(i)}\right)^{-1} \mathbf{r}_{\text{aug}}^{(i)}. \tag{26}$$

3.4) Update the state variables:

$$\hat{\mathbf{x}}^{(i)(j+1)} = \hat{\mathbf{x}}^{(i)(j)} + \Delta\hat{\mathbf{x}}^{(i)(j)}. \tag{27}$$

3.5) If $\Delta\hat{\mathbf{x}}^{(i)(j)} > \tau$, set $j \leftarrow j + 1$ then back to step 3.2. Otherwise, set $\hat{\mathbf{x}}^{(i)+} = \hat{\mathbf{x}}^{(i)(j)}$, and proceed to Step 3.6.

3.6) Compute the covariance matrix of the state estimates:

$$\mathbf{P}^{(i)+} = \left(\left(\tilde{\mathbf{H}}^{(i)(j)}\right)^T \left(\tilde{\mathbf{R}}^{(i)}\right)^{-1} \tilde{\mathbf{H}}^{(i)(j)} \right)^{-1} = \left(\tilde{\mathbf{G}}^{(i)(j)}\right)^{-1}. \tag{28}$$

3.7) Obtain the state variable $\hat{\mathbf{x}}_{(N)}^{(i)+}$ at the last time step from $\hat{\mathbf{x}}^{(i)+}$, and obtain the corresponding sub-matrix $\mathbf{P}_{(N)}^{(i)+}$ from $\mathbf{P}^{(i)+}$. When the next SW-IEKF is initiated, they serve as inputs for $\hat{\mathbf{x}}_{(0)}^{(i)+}$ and $\mathbf{P}_{(0)}^{(i)+}$.

3.8) Compute the normalized residuals of measurements using posteriori state variable $\hat{\mathbf{x}}^{(i)+}$ and covariance matrix $\mathbf{P}^{(i)+}$ as follows:

$$\hat{\mathbf{H}}^{(i)} = \frac{\partial \bar{\mathbf{h}}^{(i)}\left(\hat{\mathbf{x}}^{(i)+}, \tilde{\mathbf{u}}\right)}{\partial \hat{\mathbf{x}}^{(i)+}}, \tag{29}$$

$$\mathbf{\Omega}^{(i)} = \mathbf{R} - \left(\hat{\mathbf{H}}^{(i)}\right)^T \mathbf{P}^{(i)+} \hat{\mathbf{H}}^{(i)}, \tag{30}$$

$$\hat{\mathbf{r}}^{(i)} = \left(diag\left(\mathbf{\Omega}^{(i)}\right)\right)^{-\frac{1}{2}} \left(\bar{\mathbf{z}} - \bar{\mathbf{h}}^{(i)}\left(\hat{\mathbf{x}}^{(i)+}, \tilde{\mathbf{u}}\right)\right). \tag{31}$$

By performing the above SW-IEKF for all κ modes, the optimal state estimates can be obtained for the EM algorithm.

D. Bad Data Detection and Correction

Bad data in measurements can be effectively detected and corrected using the method of the Largest Normalized Residual (LNR) method [32]. However, in the proposed EM-SW-IEKF purposed for IBRs with control mode switching, it is first necessary to differentiate whether increases in normalized residuals in the estimation result of a certain mode arise from a mode switching event or bad data in measurements. The rationale of differentiation between the two situations is as follows. If it is a mode switching event, assuming the mode of IBR switches from Mode i_1 to Mode i_2 at the M-th point in a window of length N, which means the first M measurements originate from Mode i_1, while the remaining $N-M$ measurements from Mode i_2, the normalized residuals $\hat{\mathbf{r}}^{(i_1)}$ and $\hat{\mathbf{r}}^{(i_2)}$ for both modes will be abnormally large. At this time, the normalized conditional probability $w^{(i_2)}$ is not immediately adjusted to recognize that the system is in Mode i_2. However, the conditional probability density $p\left(\tilde{\mathbf{z}} \left| c^{(i_2)} = 1\right.\right)$ increases because some measurements in this time window conform to the patterns of Mode i_2. In comparison, if it is bad data instead of a mode switching event, as the bad data points do not conform to any mode, the conditional probability densities of all modes will decrease.

Therefore, two conditions should be concurrently met to declare the detection of bad data: first, the maximum normalized residual of the current Mode i_* ($\left\|\hat{\mathbf{r}}^{(i_*)}\right\|_\infty$) exceeds the set threshold τ (e.g., $\tau = 5$, representing five times the standard deviation); second, the conditional probability densities of all modes decrease, indicating that there are measurement data that do not conform to any mode. Then, the bad data can be eliminated or corrected using the following formula:

$$u = \arg\max_j \left\{ \left| \hat{\mathbf{r}}_j^{(i_*)} \right| \right\}, \bar{\mathbf{z}}^u \leftarrow \bar{\mathbf{z}}^u - \frac{\mathbf{R}^{uu}}{\left(\mathbf{\Omega}^{(i^*)}\right)^{uu}} \hat{\mathbf{r}}_u^{(i_*)}. \tag{32}$$

After bad data are corrected or ignored, the IEKF is performed again, ultimately yielding a state estimation result where no bad data is detected. On the other hand, if a possible mode switching is detected, bad data detection and correction are disabled during the current and subsequent cycles.

E. Summary

The introduction and derivation of the proposed EM-SW-IEKF method shown in Fig. 1 have been completed. It can be clearly observed that the SW-IEKF algorithm, corresponding to steps 3 to 8 as described in Section II-C is part of the Maximization step of the EM algorithm for iteratively solving the maximum likelihood estimation problem (8). The EM algorithm also encompasses corresponding to steps 9 to 11 for the Expectation step (13) and the other part of the Maximization step (19), as described in Section II-A, which is primarily used for calculating membership probabilities. The bad data detection and correction described in Section II-D is executed between steps 12 and 13. It can be found that for the DSE and mode detection of an IBR with multiple control modes, the state estimates of each possible mode under the current measurement set can be obtained by first performing SW-IEKF. Afterwards, using the EM algorithm, assuming equal prior probabilities for each mode (since we have no prior

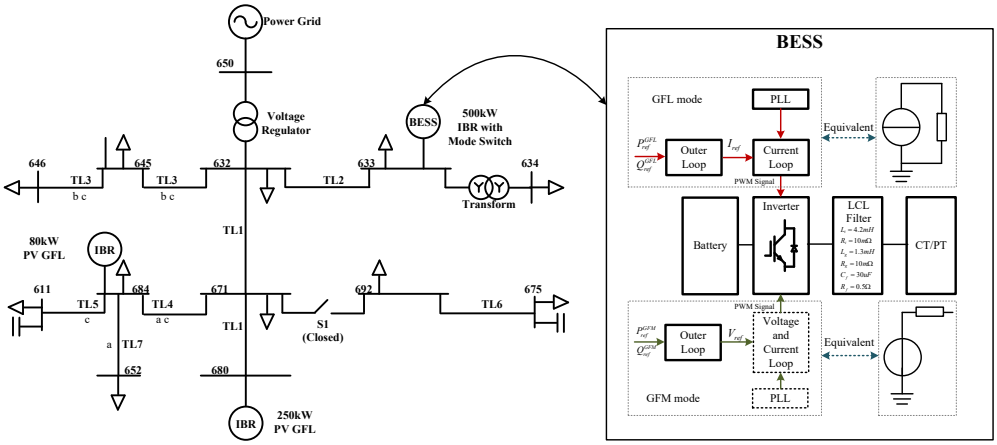

Fig. 2. One-line diagram of IEEE 13-node test feeder with 3 IBRs.

knowledge to determine which mode is currently active), the membership probabilities for each mode are calculated using the state estimates. The mode with the highest membership probability is considered to be the most likely current operating mode of the IBR, and its corresponding state estimates are taken as the final DSE results (i.e., the state estimates of unlikely modes are disregarded).

III. Simulation Results

This section will verify the proposed method on multiple test systems. First, it will be verified on a BESS in the IEEE 13-node test feeder. The test scenario is the switching between the GFM mode and the GFL mode, wherein the definition and number of state variables are completely different between these two control modes. Then, it will be verified on a PV inverter in the IEEE 34-node test feeder. The test scenario is the switching between the normal operation (Maximum Power Point Tracking, MPPT) mode and the LVRT mode, these two modes have similar structures but differ only in the number of state variables (some state locked in the LVRT mode). The detailed state-space equations of all the IBR control modes are provided in Appendix.

The true state of the system is simulated via Simulink (Version 10.5, R2022a), and the EM-SW-IEKF algorithms are implemented in MATLAB (Version 9.12, R2022a). The measurement sampling frequency is 3840 Hz, i.e., 64 points per cycle, a specification easily met by merging units (MUs), digital fault recorders (DFRs), and smart inverters. It is worth noting that for DSE purposes, both MUs and DFRs have been extensively discussed in existing literature [33]. Moreover, the recent IEEE standard recommends smart inverters to provide data output capabilities that can be used for DSE [34] .

A. Case 1: Switching between GFM and GFL Modes

In the modified IEEE 13-node test feeder shown in Fig. 2, three IBRs integrated into the system include two PV generation systems operating in the GFL mode and one BESS capable of switching between the GFL and GFM modes.

For the BESS, regardless of whether it is in the GFL mode or in the GFM mode, a set of voltage references is generated and converted into Pulse Width Modulation (PWM) signals to drive the inverter. The control mode selection is performed by choosing the appropriate PWM signals from the two control modes. Regardless of how the control mode changes, it can be observed that the model and parameters of the physical subsystem remain unchanged. For the control subsystem, its dynamics conform to the form of (3), hence the proposed EM-SW-IEKF method can be used for control mode switching detection and DSE.

Initially, the BESS operates in the GFM mode with Virtual Synchronous Generator (VSG) control. At 2s, a transition is made from the GFM mode to the GFL mode, where the active power reference value (0.7 p.u.) and reactive power reference value (0 p.u.) are directly specified in the GFL mode. At 3s, the active power reference in the GFL mode changes to 0.6 p.u.; at 5s, a transition back to the GFM mode occurs; and from 8s to 8.1s, the system frequency drops from 60Hz to 59.75Hz and remains at 59.75Hz until the simulation ends. The total simulation time is 10s. It is important to clarify that in reality, control mode switching and system disturbance events do not occur as frequently as demonstrated in the simulation. The use of specific simulation conditions and parameters is primarily to verify the accuracy and reliability of the proposed method within the constraints of limited computational resources. In order to test the proposed method under bad data, at 1.25s (GFM mode), V_{iq}^{c} is observed to have abnormal values (0 p.u.) at three consecutive sampling points; at 4s, uniformly changing abnormal values (from 0.3 p.u. to 0) are observed in V_{id}^{c} over four consecutive points.

1) Seamless transition method: As shown in Fig. 2, the IBR needs to select a set of voltage reference signals to drive the inverter. When a control mode switching occurs, if there is a significant difference between the two sets of voltage references signals, it will generate a large disturbance. To avoid such disturbances, a transition process can be implemented, allowing the switching to be made when the outputs of the two modes are the same. There are currently several methods for transition between GFM and GFL modes [35]. A general disturbance-free and delay-free transition scheme has been used to achieve this transition [36].

The control block diagrams, state variables, and parameters of the GFL and GFM modes are shown in Fig. 3. It is observed that the GFM mode has morestate variables and parameters, as well as more complex control logic, compared with the GFL

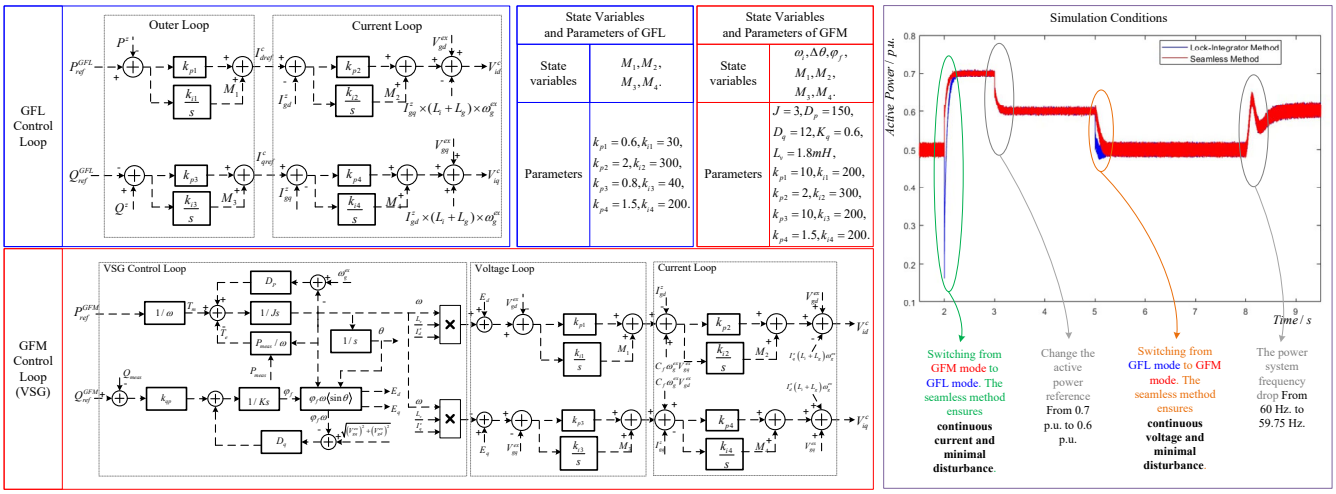

Fig. 3. Control block diagrams, dynamic state variables, parameters, and mode switching for the GFL mode and the GFM mode.

mode. In GFL mode, the state variables are mainly created by the integrators in the PI blocks, $M_1 - M_4$, while in the GFM mode, there are also the equivalent angular frequency ω_i, the power angle $\Delta\theta$, and the flux linkage φ_f from the VSG. Apart from the PI parameters, the GFM mode also introduces additional parameters such as the virtual inertia coefficient J and the virtual impedance L_v, compared to the GFL mode.

When an IBR operates in one control mode, the other idle mode does not output voltage references for closed-loop control; hence, a relatively simple method is to lock all PI blocks of the idle mode. Using this method, if the idle mode is not activated in advance when a mode switch occurs, directly switching will result in disturbances. The newly proposed method in [36] adjusts the references tracked by the idle mode to make its output the same as the active mode, thus making the idle mode a *standby mode* for seamless switching. When the IBR operates in the GFL mode, the GFM mode operates as the standby mode, shifting from tracking the power reference to tracking the voltage of the PCC, so that when the switch occurs, the voltage at the PCC does not change abruptly. Similarly, when the IBR operates in the GFM mode, the GFL mode operates as the standby mode, shifting from tracking the power reference to tracking the current of the PCC, so that when the switch occurs, the current at the PCC does not change abruptly.

Simulation results, as shown in Fig. 3, reveal that the seamless switching method achieves negligible disturbances when switching between the two modes, significantly outperforming the lock-integrator method. Additionally, at 3s, the GFL mode effectively tracks the changes in the active power reference; at 8s, as the transmission system frequency decreases, the BESS operates like a SG, using inertia to provide active power support, thanks to the VSG control. Both modes function correctly, setting the stage for verification of the proposed method for control mode switching detection and DSE. A simulation of 8.5s real time is completed in 4.96 seconds, with the VSG part taking 3.04 seconds and the GFL part taking 1.92 seconds, meeting the real-time requirements.

2) Control mode switching detection: As described in Section II, the proposed EM-SW-IEKF algorithm first applies SW-

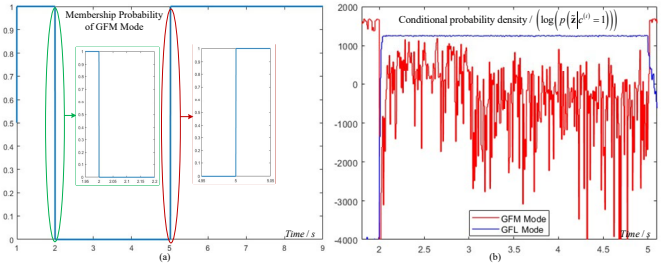

Fig. 4. Control mode switching detection: between GFM and GFL modes.

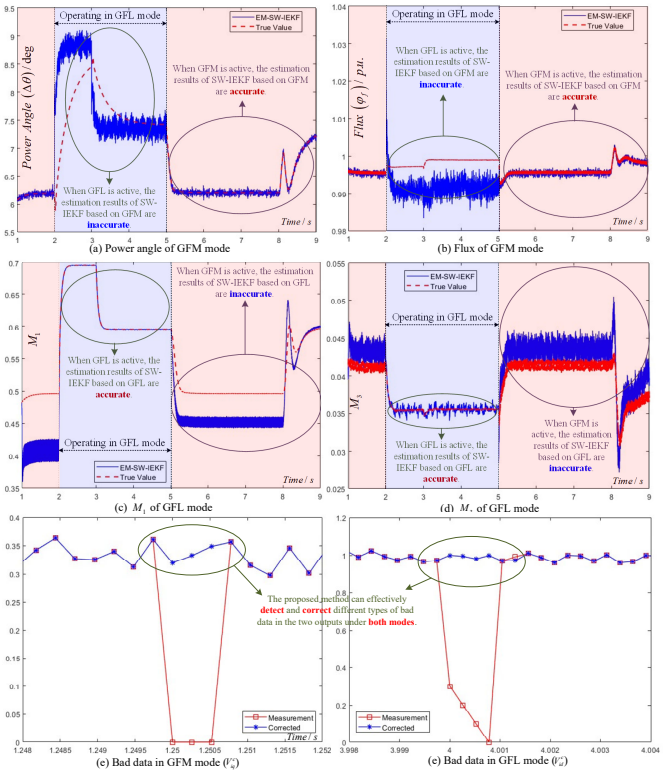

Fig. 5. DSE results and bad data correction when BESS switches between GFL and GFM modes.

IEKF to all possible modes, then calculates the membership probability for each mode. In the case of switching between GFM and GFL modes, there are only two possible modes. Therefore, it can be considered that the mode with the higher membership probability is the active mode that controls the inverter, while the mode with the lower membership probability is the standby mode.

The length of the sliding window affects the performance of the algorithm. Considering that mode switches do not occur frequently in practice, the EM-SW-IEKF algorithm is performed every 32 points (i.e., half a cycle) here. For the measured voltage reference values (V_{id}^c and V_{iq}^c), i.e., the controller outputs, Gaussian noise $N\left(0, 0.1^2\right)$ is added. Given that the nonlinearity and complexity of the GFM mode are significantly higher than those of the GFL mode, more process noise is introduced during the discretization process. Therefore, $\mathbf{Q}^{(GFM)}$ is set to $2 \times 10^{-7}\mathbf{I}$ and $\mathbf{Q}^{(GFL)}$ is set to $1 \times 10^{-8}\mathbf{I}$.

Simulation results, as shown in Fig. 4 (a), reveal that the membership probabilities obtained through the EM-SW-IEKF algorithm can effectively reflect the current operating mode of the IBR. The *conditional probability density* between 2-5 seconds is shown in Fig. 4 (b). Simulation results indicate that at 2.01s, the conditional probability density of the GFL mode exceeds that of the GFM mode for the first time. After 5s, the conditional probability density of the GFM mode exceeds that of GFL mode. Note that the other events introduced in the simulation (active power reference change at 3s and frequency disturbance at 8s) do not affect the result of the model switching detection, demonstrating that the proposed method is highly robust.

3) DSE: Fig. 5 (a) and (b) present the estimation results of state variables $\Delta\theta$ and φ_f under the GFM mode. For a VSG, which simulates SG operation, the virtual power angle and flux linkage are considered very critical variables to track. It is observed that when the IBR operates in the GFM mode, the SW-IEKF for the GFM mode estimates them accurately; whereas when the IBR operates in the GFL mode, the SW-IEKF for the GFM mode produces results that are not meaningful, because the IBR is not actually controlled by the standby GFM mode. Because the proposed algorithm correctly detects that the system actually operates in the GFL mode (Fig. 4), the DSE results for the GFM mode will be disregarded.

Similarly, estimation results for some state variables (M_1 and M_3) under the GFL mode are shown in Fig. 5 (c) and (d). When the IBR operates in GFL mode, the SW-IEKF for the GFL mode estimates them accurately; when the IBR operates in the GFM mode, the estimation results for these variables are not meaningful and will be automatically disregarded.

Fig. 5 (e) and (f) illustrate the bad data detection and correction performed by the proposed method. It is observed that under different modes and when encountering various types of bad data in different outputs, effective detection and correction are achieved by the method. No adverse impact on the DSE results or mode detection results is caused by using the corrected measurements.

In conclusion, for a BESS with both GFM and GFL control modes, the EM-SW-IEKF method enables accurate detection of the control mode switching jointly with the estimation of state variables of the active control mode.

B. Case 2: Switching between Normal and LVRT Modes

The control subsystem of an IBR contains numerous PI blocks. To prevent overflow in the integrators within these PI blocks under abnormal operating conditions, limiters should be imposed. When the integrators reach their limit, the IBR state transition equation undergoes a change, with a reduced number of dynamic state variables, which cannot be handled by traditional DSE methods for IBRs without considering limiters. LVRT represents a typical scenario that triggers current limitations. To maintain the same power output when the voltage at the PCC drops, an increase in current is necessary. The current output capacity of an IBR is finite, primarily determined by the overcurrent capacity of IGBTs. To ensure the low-voltage ride-through, the current must be limited. Additionally, when the voltage at the PCC point drops, increasing the reactive power output of the IBR to support the grid voltage can further reduce the limit of active current. In this section, we will demonstrate that the proposed EM-SW-IEKF method is capable of detecting the event ofan IBR entering the LVRT mode, while also performing DSE for the IBR in both the LVRT mode and the normal operation mode.

Here, we will present results for a PV system connected to the more complex IEEE 34-node test feeder. The system one-line diagram and the control block diagram of the PV system are shown in Fig. 6 (a). EM-SW-IEKF is performed on an IBR with a rated power of 500 kW connected to node 850. Other components incorporated into the test feeder include two PV inverters operating in the GFL mode, one BESS operating in the GFM mode, and two dynamic loads [37].

Assuming the overcurrent capability of the IGBT is 1.2 p.u., to maintain a certain margin, the current limit $I_{\lim}$ is set to 1.05 p.u. Compared with IBRs operating in the MPPT mode, the LVRT mode mainly introduces two additional features. 1) Reactive power control capability. Here, the reactive power curve is designed in three segments. When the PCC voltage ($|V_{PCC}|$) is below 0.7 p.u., the reactive power reference is set to $1.05\,|V_{PCC}|$, with the IBR striving to output maximum reactive power; when the $|V_{PCC}|$ is between 0.7 p.u. and 0.85 p.u., the reactive reference is kept constant at 0.735 p.u.; when the PCC voltage is above 0.85 p.u., the reactive reference decreases linearly until the voltage exceeds 0.95 p.u., after which the reactive reference becomes zero. 2) Current limitation. The total current should be below $I_{\lim}$, thus the active current reference is limited.

In the simulation, the irradiance is set to 900 W/m^2 (the corresponding active power is 0.92 p.u.). The measurement noise of the voltage reference is the same as in Case 1, being Gaussian noise with a distribution of $N\left(0, 0.1^2\right)$. The MPPT mode and LVRT mode differ only in that one integrator is limited, and their structure is similar to the GFL mode in Case 1. Therefore, $\mathbf{Q}$ for both modes are set to $1 \times 10^{-8}\mathbf{I}$. At 2s, the transmission system voltage starts to drop from 1.0 p.u., reaching 0.6 p.u. by 2.5s. At 4.5s, the transmission system voltage begins to recover, returning to 0.98 p.u. by 5.5s. The power output (both active and reactive power) of the IBR

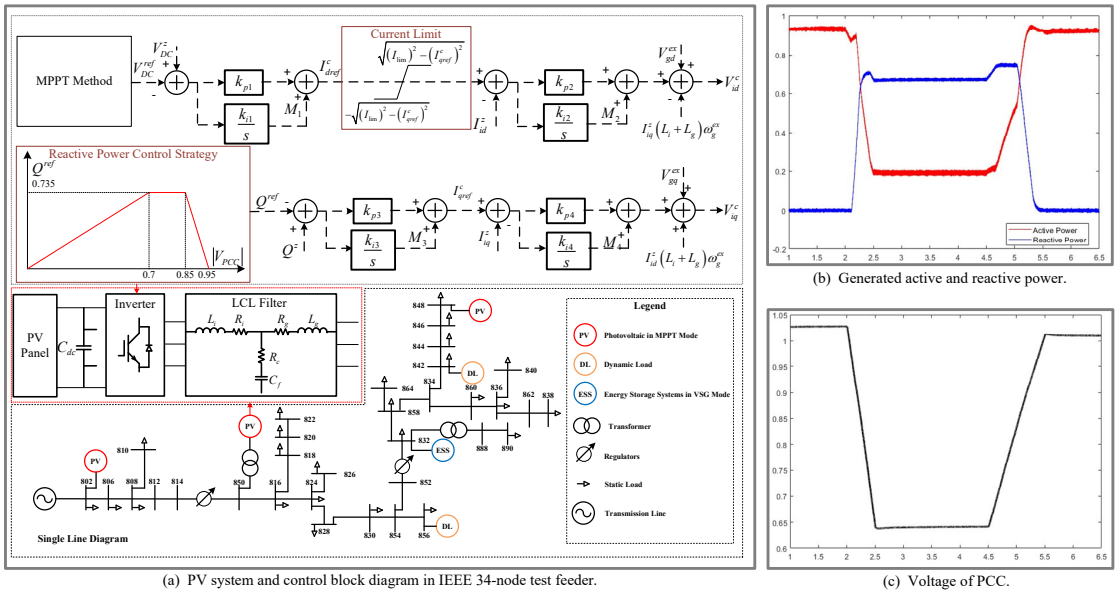

(a) PV system and control block diagram in IEEE 34-node test feeder.

(b) Generated active and reactive power.

(c) Voltage of PCC.

Fig. 6. Control block diagram of a PV system in the IEEE 34-node test feeder and operating conditions.

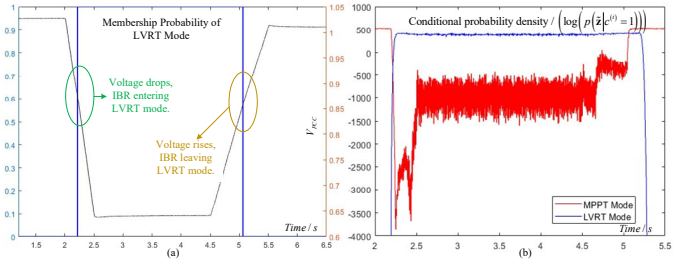

Fig. 7. Simulation results of mode detection during the switching between LVRT and MPPT modes.

and the voltage of the PCC (voltage at node 850) are shown in Fig. 6 (b) and (c). It is observed that as the transmission system voltage decreases, the IBR increases its reactive power output. When the voltage falls below 0.7 p.u., the reactive power drops due to current limitations, maintaining a constant reactive current. The active power is limited by the current. The operation of the IBR conforms to the design. A simulation of 5.5s real time is completed in 2.16 seconds, with the MPPT part taking 1.18 seconds and the LVRT part taking 0.98 seconds, meeting the real-time requirements.

1) Control mode switching detection: Fig. 7 (a), shows that before the voltage drop, the IBR operates in the MPPT mode, with active power output close to 0.9 p.u., leading to rapid saturation of the current as the voltage decreases, triggering the LVRT mode. The conditional probability density from 2s to 5.5s is shown in Fig. 7 (b). It can be observed that at 2s, the conditional probability density of the MPPT mode rapidly decreases. However, the rise in conditional probability density for the LVRT mode takes some time, and at 2.2s, the system is determined to have entered LVRT mode. This slight delay in mode detection is due to the initial values of the dynamic state variables in the LVRT mode having significant errors, requiring time to track the actual dynamic state. Similarly, as the voltage rises, at 5.06s, the IBR is determined to resume operation in the MPPT mode.

2) DSE: In Case 1 with the switching between GFM and GFL modes, due to the significant differences in the two control modes, the definition and the number of state variables are largely different. However, in the switching between the LVRT and normal operation (MPPT) modes, the overall control does not undergo significant changes, but some state variables become irrelevant due to saturation, leading to a change in the number of state variables. Taking the system shown in Fig. 6 as an example, when operating in the MPPT mode, there are four dynamic state variables, $M_1 - M_4$. When the IBR enters LVRT mode, M_1 is limited, leaving only $M_2 - M_4$ as the state variables. Consequently, the corresponding state transition equations and output equations also change.

Due to the decoupled control adopted by the PV system, the state variables (M_3 and M_4) are related to reactive power control and their control blocks remain the same under the normal (MPPT) mode and the LVRT mode. Thus, when the IBR operates in the LVRT mode, the SW-IEKF for both modes achieve good DSE results, as shown in Fig. 8 (c) and (d). When the IBR operates in the normal (MPPT) mode, the estimation by the SW-IEKF for the LVRT mode exhibits a minor error. This is because the LVRT mode only has three state variables, while there are actually four state variables at this time, leading IEKF to converge to an approximate but inaccurate result. For the state variable related to active power control, as shown in Fig. 8 (a), M_1 is only relevant in the normal (MPPT) mode, and when the IBR operates in the MPPT mode, the SW-IEKF of the MPPT mode also achieves accurate estimation results. For M_2, as shown in Fig. 8 (b), it is observed that when the IBR operates in the LVRT mode, the estimation result of the SW-IEKF of the MPPT mode shows significant error, while SW-IEKF of the LVRT mode estimates accurately; when the IBR operates in the MPPT mode, SW-IEKF of the MPPT mode obtains accurate estimation results. Overall, as the results of the SW-IEKF corresponding to the mode with the highest membership probability (see Fig. 7) is selected as the final DSE result, the estimation is accurate through the

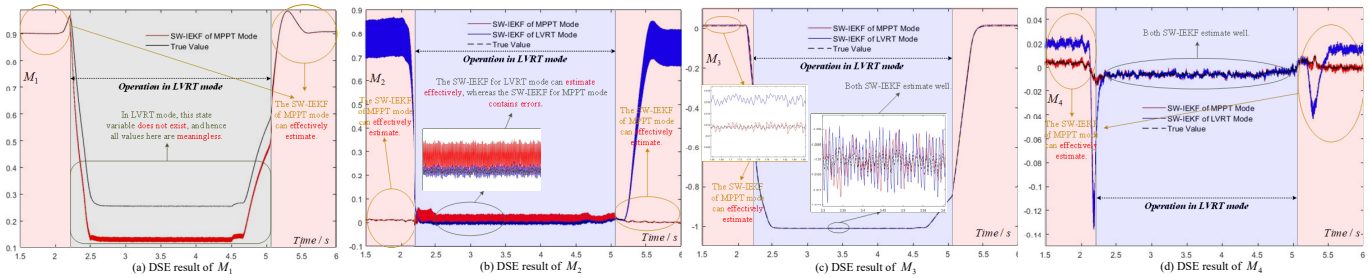

Fig. 8. DSE results when the solar PV system switches between MPPT and LVRT modes.

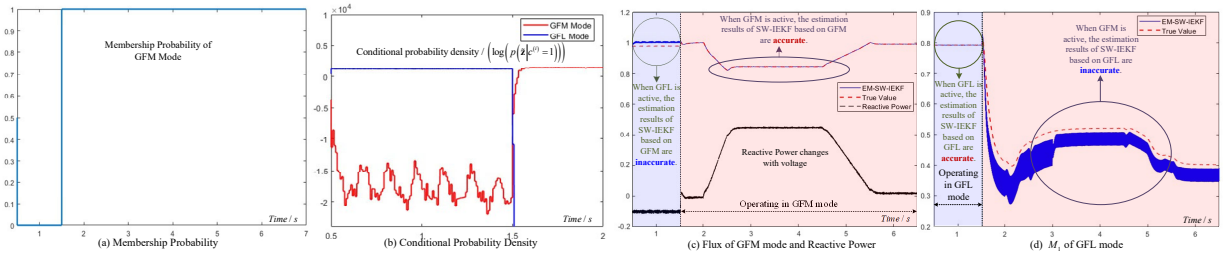

Fig. 9. Mode detection and DSE results of BESS at node 832.

entire simulation peoriod with control mode switching.

3) Influence among multiple IBRs: To better validate the versatility of the proposed method under conditions where multiple IBRs are connected to the power system with mode switching, the BESS at node 832 is switched from GFL mode to GFM mode at 1.5s based on the previous experiments. The two control modes utilized by this IBR are the same as those in Fig. 3. As the voltage of the transmission system decreases, an increase in the reactive power output of the BESS is observed.

The mode detection result and the conditional probabilities of the two modes are shown in Fig. 9 (a) and (b). It can be observed that the proposed method still effectively accomplishes mode detection. The DSE results are presented in Fig. 9 (c) and (d). It is observed that when the IBR operates in a certain mode, the proposed method effectively tracks the state variables corresponding to that mode.

Furthermore, since the EM-SW-IEKF method is applied to a single IBR using its own measurements, the complexity of the power system and the number of IBRs do not affect the proposed method. Possible interactions among multiple IBRs are present as potential inputs in the DSE process. It is observed that there is no impact between the DSE of the BESS and that of the PV unit connected to node 850.

IV. Conclusion

A novel switching DSE method for IBRs with multiple control modes is proposed in this paper. This is motivated by the fact that the multiplicity of IBR control modes of IBRs may render conventional DSE methods with the assumption of a single system model ineffective. The proposed EM-SW-IEKF method utilizes the EM algorithm for the estimation of the probabilities of each control mode, leading to the detection of control mode switching. It is remarkable that the most intensive step of the EM algorithm is equivalent to the standard SW-IEKF method for each mode, which significantly facilitates the algorithmic implementation and the ease of computation. Simulations demonstrate the capabilities of the proposed method in IBRs with typical scenarios of control mode switchings.

As an emerging topic, DSE for IBRs requires further exploration, and future work may include the use of the proposed method to detect faults and cyber attacks, and the extension of the proposed method to IBR model identification. Additionally, considering that the proposed EM-SW-IEKF method requires comprehensive knowledge of the IBR model, which may not always be fully available to power system operators from IBR manufacturers. Even though generic IBR models and system identification methods could be applied, future work may also involve the combination of data-driven modeling with the proposed switching DSE method.

References

[1] M. Nehrir, C. Wang, K. Strunz, H. Aki, R. Ramakumar, J. Bing, Z. Miao, and Z. Salameh, "A review of hybrid renewable/alternative energy systems for electric power generation: Configurations, control, and applications," *IEEE transactions on sustainable energy*, vol. 2, no. 4, pp. 392–403, 2011.

[2] Q. Peng, Q. Jiang, Y. Yang, T. Liu, H. Wang, and F. Blaabjerg, "On the stability of power electronics-dominated systems: Challenges and potential solutions," *IEEE Transactions on Industry Applications*, vol. 55, no. 6, pp. 7657–7670, 2019.

[3] Y. Li, Y. Gu, and T. C. Green, "Mapping of dynamics between mechanical and electrical ports in sg-ibr composite grids," *IEEE Transactions on Power Systems*, vol. 37, no. 5, pp. 3423–3433, 2022.

[4] C. Wang, Z. Qin, Y. Hou, and J. Yan, "Multi-area dynamic state estimation with pmu measurements by an equality constrained extended kalman filter," *IEEE Transactions on Smart Grid*, vol. 9, no. 2, pp. 900–910, 2016.

[5] S. Yu, K. Emami, T. Fernando, H. H. Iu, and K. P. Wong, "State estimation of doubly fed induction generator wind turbine in complex power systems," *IEEE Transactions on Power Systems*, vol. 31, no. 6, pp. 4935–4944, 2016.

[6] F. Bakhtiari and J. Nazarzadeh, "Optimal estimation and tracking control for variable-speed wind turbine with pmsg," *Journal of modern power systems and clean energy*, vol. 8, no. 1, pp. 159–167, 2019.

[7] S. Huang, T. Wang, T. Ji, and M. Jin, "Adaptive cubature kalman filter based dynamic state estimation for grid-connected photovoltaic system," in *2021 4th International Conference on Energy, Electrical and Power Engineering (CEEPE)*. IEEE, 2021, pp. 570–575.

[8] Y. Li, L. Zhang, K. Lai, and X. Zhang, "Dynamic state estimation method for multiple battery energy storage systems with droop-based consensus control," *International Journal of Electrical Power & Energy Systems*, vol. 134, p. 107328, 2022.
[9] A. Paul, G. Joos, and I. Kamwa, "Decentralized dynamic state estimation of doubly fed induction generator using terminal measurements," in *2018 IEEE Power & Energy Society Innovative Smart Grid Technologies Conference (ISGT)*. IEEE, 2018, pp. 1–5.
[10] G. Anagnostou, L. P. Kunjumuhammed, and B. C. Pal, "Dynamic state estimation for wind turbine models with unknown wind velocity," *IEEE Transactions on Power Systems*, vol. 34, no. 5, pp. 3879–3890, 2019.
[11] H. Huang, Y. Lin, X. Lu, Y. Zhao, and A. Kumar, "Dynamic state estimation for inverter-based resources: A control-physics dual estimation framework," *IEEE Transactions on Power Systems*, pp. 1–12, 2024.
[12] J. Zhao, M. Netto, Z. Huang, S. S. Yu, A. Gómez-Expósito, S. Wang, I. Kamwa, S. Akhlaghi, L. Mili, V. Terzija *et al.*, "Roles of dynamic state estimation in power system modeling, monitoring and operation," *IEEE Transactions on Power Systems*, vol. 36, no. 3, pp. 2462–2472, 2020.
[13] K. Yue, Y. Liu, P. Zhao, B. Wang, M. Fu, and H. Wang, "Dynamic state estimation enabled health indicator for parametric fault detection in switching power converters," *IEEE Access*, vol. 9, pp. 33 224–33 234, 2021.
[14] S. Yu, L. Zhang, H. H.-C. Lu, T. Fernando, and K. P. Wong, "A dse-based power system frequency restoration strategy for pv-integrated power systems considering solar irradiance variations," *IEEE Transactions on Industrial Informatics*, vol. 13, no. 5, pp. 2511–2518, 2017.
[15] Y. Liu, S. Choi, A. S. Meliopoulos, R. Fan, L. Sun, and Z. Tan, "Dynamic state estimation enabled preditive inverter control," in *2016 IEEE Power and Energy Society General Meeting (PESGM)*. IEEE, 2016, pp. 1–5.
[16] D. Xie, Z. Xu, L. Yang, J. Østergaard, Y. Xue, and K. P. Wong, "A comprehensive lvrt control strategy for dfig wind turbines with enhanced reactive power support," *IEEE transactions on power systems*, vol. 28, no. 3, pp. 3302–3310, 2013.
[17] N. Saadat, S. S. Choi, and D. M. Vilathgamuwa, "A statistical evaluation of the capability of distributed renewable generator-energy-storage system in providing load low-voltage ride-through," *IEEE Transactions on Power Delivery*, vol. 30, no. 3, pp. 1128–1136, 2015.
[18] R. Rosso, X. Wang, M. Liserre, X. Lu, and S. Engelken, "Grid-forming converters: Control approaches, grid-synchronization, and future trends—a review," *IEEE Open Journal of Industry Applications*, vol. 2, pp. 93–109, 2021.
[19] T. Wu, M. Rothleder, Z. Alaywan, and A. Papalexopoulos, "Pricing energy and ancillary services in integrated market systems by an optimal power flow," *IEEE Transactions on Power Systems*, vol. 19, no. 1, pp. 339–347, 2004.
[20] L. Feng, X. Zhang, C. Li, X. Li, B. Li, J. Ding, C. Zhang, H. Qiu, Y. Xu, and H. Chen, "Optimization analysis of energy storage application based on electricity price arbitrage and ancillary services," *Journal of Energy Storage*, vol. 55, p. 105508, 2022.
[21] K. P. Murphy, "Switching kalman filters," 1998.
[22] F. Cai, S. Liao, Y. Chen, and W. Wang, "Kalman filter of switching system under hybrid cyber attack," *IEEE Transactions on Automation Science and Engineering*, 2023.
[23] J. Oster, J. Behar, O. Sayadi, S. Nemati, A. E. Johnson, and G. D. Clifford, "Semisupervised ecg ventricular beat classification with novelty detection based on switching kalman filters," *IEEE Transactions on Biomedical Engineering*, vol. 62, no. 9, pp. 2125–2134, 2015.
[24] C. K. R. Lim and D. Mba, "Switching kalman filter for failure prognostic," *Mechanical Systems and Signal Processing*, vol. 52, pp. 426–435, 2015.
[25] H. Shiri, J. Wodecki, and R. Zimroz, "Robust switching kalman filter for diagnostics of long-term condition monitoring data in the presence of non-gaussian noise," in *IOP Conference Series: Earth and Environmental Science*, vol. 1189, no. 1. IOP Publishing, 2023, p. 012007.
[26] R. Brijder, S. Helsen, and A. P. Ompusunggu, "Switching kalman filtering-based corrosion detection and prognostics for offshore wind-turbine structures," *Wind*, vol. 3, no. 1, pp. 1–13, 2023.
[27] G. Nguyen-Quynh, P. Becker, C. Qiu, M. Rudolph, and G. Neumann, "Switching recurrent kalman networks," *arXiv preprint arXiv:2111.08291*, 2021.
[28] E. Pei, X. Xia, L. Yang, D. Jiang, and H. Sahli, "Deep neural network and switching kalman filter based continuous affect recognition," in *2016 IEEE International Conference on Multimedia & Expo Workshops (ICMEW)*. IEEE, 2016, pp. 1–6.
[29] M. Khodarahmi and V. Maihami, "A review on kalman filter models," *Archives of Computational Methods in Engineering*, vol. 30, no. 1, pp. 727–747, 2023.
[30] A. Gelb *et al.*, *Applied optimal estimation*. MIT press, 1974.
[31] H. W. Sorenson, "Least-squares estimation: from gauss to kalman," *IEEE spectrum*, vol. 7, no. 7, pp. 63–68, 1970.
[32] Y. Lin and A. Abur, "A highly efficient bad data identification approach for very large scale power systems," *IEEE Transactions on Power Systems*, vol. 33, no. 6, pp. 5979–5989, 2018.
[33] Y. Liu, A. K. Singh, J. Zhao, A. S. Meliopoulos, B. Pal, M. A. bin Mohd Ariff, T. Van Cutsem, M. Glavic, Z. Huang, I. Kamwa *et al.*, "Dynamic state estimation for power system control and protection," *IEEE Transactions on Power Systems*, vol. 36, no. 6, pp. 5909–5921, 2021.
[34] D. G. Photovoltaics and E. Storage, "Ieee standard for interconnection and interoperability of distributed energy resources with associated electric power systems interfaces," *IEEE Std*, pp. 1547–2018, 2018.
[35] W. Wang, K. Sun, K.-J. Li, Y. Dong, Z. Zhang, and Y. Sun, "Smooth switching control strategy with complete process of frequency support for photovoltaic grid-connected converter," *International Journal of Electrical Power & Energy Systems*, vol. 151, p. 109177, 2023.
[36] Y. L. X. L. Heqing Huang, Lizhi Ding and Y. Zheng, "A seamless transition between grid-forming and grid-following controls of inverter-based resources (accepted)," in *2024 IEEE Energy Conversion Congress and Exposition (ECCE)*, 2024.
[37] D. Hill, "Nonlinear dynamic load models with recovery for voltage stability studies," *IEEE Transactions on Power Systems*, vol. 8, no. 1, pp. 166–176, 1993.

APPENDIX

The state transition equations and output equations of the four different control modes of the IBRs used in this paper are shown in Fig. 10. Since all the IBRs are voltage source inverters, the output variables consist of two components, namely the voltage references in the dq-axis (V_{id}^c and V_{iq}^c indicated in red in the figure). The state variables at the current time step are indicated in blue. In Case 1, the GFM mode contains seven state variables, including angular frequency ω_i, power angle $\Delta\theta$, flux linkage φ_f and the outputs of four integrators (M_1 to M_4). The state variables in the other three GFL modes are all the outputs of the integrators (M_1 to M_4), and due to the current outer loop being limited under LVRT, there are only three state variables (M_2 to M_4).

The sampling interval is represented by Δt, w denotes the process noise, and v denotes the output noise. The state variables shown in green represent the predicted values for the next time step, calculated based on the discrete state transition equations.

The definitions of the relevant parameters for the two modes in Case 1 are as follows: J_p represents the inertia constant; D_p and D_q represent the damping coefficients for active and reactive power, respectively; K_q represents the reactive power coefficient; L_v denotes the virtual impedance of the VSG; k_{p1} to k_{p4} and k_{i1} to k_{i4} represent the PI parameters of the four PI blocks; L_i, L_g and C_f represent the inductance on the inverter side, the inductance on the grid side, and the filter capacitance of the LCL filter, respectively.

The relevant external inputs of Case 1 are defined as follows: P_{GFM}^{ref} and P_{GFM}^{ref} represent the active power reference and reactive power reference in GFM mode, respectively; P_{GFL}^{ref} and Q_{GFL}^{ref} represent the active power reference and reactive power reference in GFL mode, respectively; ω_g^{ex} represents the grid angular frequency obtained from the PLL; V_{gd}^{ex} and V_{gq}^{ex} are the grid voltage measurements; I_{gd}^{ex}, I_{gq}^{ex},

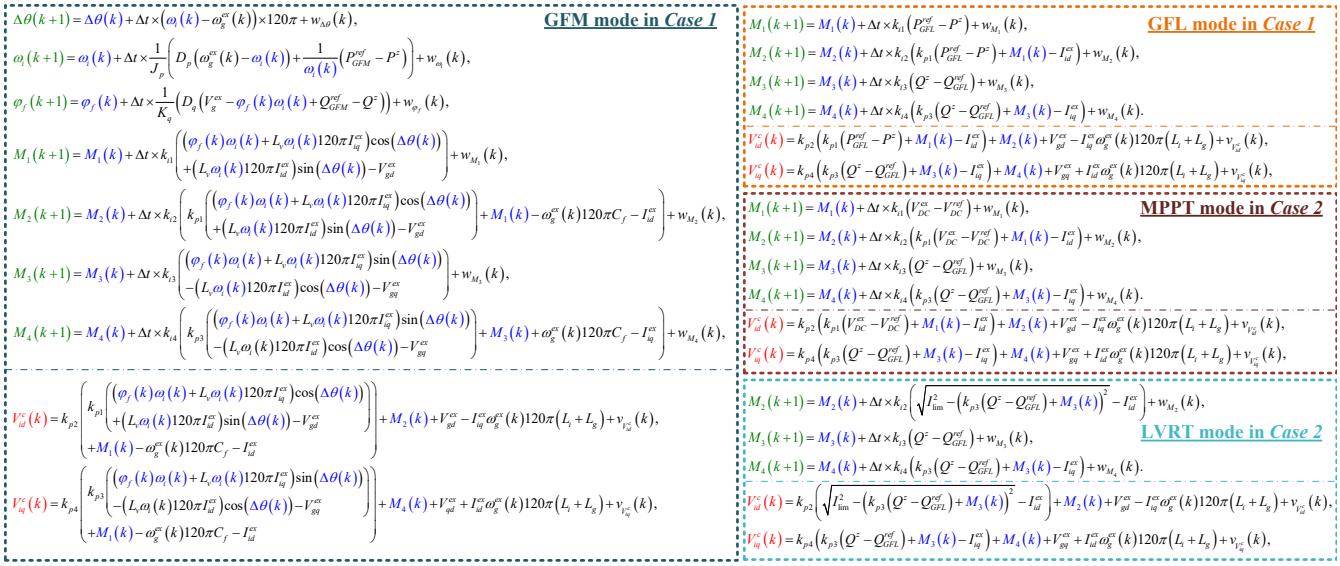

Fig. 10. State transition equations and output equations in this paper.

I_{id}^{ex}, and I_{iq}^{ex} are the current measurements on the grid side and inverter side, respectively. Finally, P^z, Q^z, and V_{iq}^z represent the active power, reactive power, and voltage.

The definitions of the relevant parameters for the two modes in Case 2 are as follows: k_{p1} to k_{p4} and k_{i1} to k_{i4} represent the PI parameters of the four PI blocks; L_i and L_g represent the inductance on the inverter side and grid side of the LCL filter, respectively; I_{lim} represents the current limit.

The relevant external inputs of Case 2 are defined as follows: V_{DC}^{ref} represents the DC voltage reference obtained from the MPPT algorithm; Q_{GFL}^{ref} represents the reactive power reference; ω_g^{ex} represents the grid angular frequency obtained from the PLL; V_{gd}^{ex} and V_{gq}^{ex} are the grid voltage measurements; I_{gd}^{ex}, I_{gq}^{ex}, I_{id}^{ex}, and I_{iq}^{ex} are the current measurements on the grid side and inverter side, respectively; V_{DC}^{ex} represents the voltage measurement of the DC capacitor. Finally, P^z and Q^z represent the active power and reactive power calculated from the above measurements.